

IPN-V2 and OCTA-500: Methodology and Dataset for Retinal Image Segmentation

Mingchao Li, Yuhan Zhang, Zexuan Ji, Keren Xie, Songtao Yuan, Qinghui Liu and Qiang Chen

Abstract—Optical coherence tomography angiography (OCTA) is a novel imaging modality that allows a micron-level resolution to present the three-dimensional structure of the retinal vascular. In our previous work, a 3D-to-2D image projection network (IPN) was proposed for retinal vessel (RV) and foveal avascular zone (FAZ) segmentations in OCTA images. One of its advantages is that the segmentation results are directly from the original volumes without using any projection images and retinal layer segmentation. In this work, we propose image projection network V2 (IPN-V2), extending IPN by adding a plane perceptron to enhance the perceptron ability in the horizontal direction. We also propose IPN-V2+, as a supplement of the IPN-V2, by introducing a global retraining process to overcome the "checkerboard effect". Besides, we propose a new multi-modality dataset, dubbed OCTA-500. It contains 500 subjects with two field of view (FOV) types, including OCT and OCTA volumes, six types of projections, four types of text labels and two types of pixel-level labels. The dataset contains more than 360K images with a size of about 80GB. To the best of our knowledge, it is currently the largest OCTA dataset with the abundant information. Finally, we perform a thorough evaluation of the performance of IPN-V2 on the OCTA-500 dataset. The experimental results demonstrate that our proposed IPN-V2 performs better than IPN and other deep learning methods in RV segmentation and FAZ segmentation.

Index Terms—Image databases, segmentation, multimodal systems, network architecture and design

1 INTRODUCTION

Optical coherence tomography (OCT) is one of the most significant advances in retinal imaging, as it non-invasively captures 3D structural data of the retina with micron-level resolution [1]. OCT helps doctors observe the cross-sectional structure of the retina and monitor fluid leakage, but cannot directly provide blood flow information. Building on the OCT platform, OCT angiography (OCTA) has been developed as a new useful imaging modality for providing functional information of retinal blood vessels and microvascular systems [2].

Compared with traditional angiographies, such as fluorescein angiography and indocyanine green angiography, OCTA is a novel non-invasive technique that only takes a few seconds to acquire retinal angiography volume. Besides, the OCTA volumetric data can be projected from different retinal layers to enable separate visualization of the

corresponding retinal plexuses. This unique observation perspective improves our understanding of the pathophysiology of retinal vasculature. Many studies [2], [3], [4], [5] have demonstrated the significant role of OCTA in the evaluation of retinal vascular diseases such as age-related macular degeneration (AMD), diabetic retinopathy (DR), choroidal neovascularization (CNV), uveitis, inherited diseases, artery and vein occlusions, and glaucomatous.

The study of OCTA images has received a lot of attention, and current researches mainly focus on quantifying useful information to assist clinical assessment. Many works have been developed, such as retinal vessel (RV) segmentation [6], [7], [8], [9], foveal avascular zone (FAZ) segmentation [10], [11], [12], [13], non-perfusion area segmentation [14], [15], CNV segmentation [16], [17], [18], [19], etc. In particular, RV and FAZ are the common structures that exist in every retina, and they have the most intuitive changes when retinal diseases occur [20], [21], [22]. As basic studies, the RV segmentation and the FAZ segmentation are necessary but also challenging.

As shown in Fig.1, the challenges of the RV segmentation and the FAZ segmentation include (1) Error layer segmentation. Several diseases can destroy the structure of the retinal layer, and sometimes lead to poor layer segmentation, which in turn affects the performance of the target segmentation algorithms. (2) Interference of similar structure. The grayscale values of the non-perfusion and the FAZ are similar and sometimes difficult to be distinguished. (3) Poor imaging quality. The turbid refractive medium and image noise will cause unclear imaging and inaccurate segmentation boundaries.

- M.C. Li is with the School of Computer Science and Engineering, Nanjing University of Science and Technology, Nanjing 210094, China. E-mail: chaosli@njust.edu.cn.
- Y.H. Zhang is with the School of Computer Science and Engineering, Nanjing University of Science and Technology, Nanjing 210094, China. E-mail: zhangyuhan@njust.edu.cn.
- Z.X. Ji is with the School of Computer Science and Engineering, Nanjing University of Science and Technology, Nanjing 210094, China. E-mail: jizexuan@njust.edu.cn.
- K.R. Xie is with Department of Ophthalmology, The First Affiliated Hospital with Nanjing Medical University, Nanjing 210029, China. E-mail: mark19900209@163.com.
- S.T. Yuan is with Department of Ophthalmology, The First Affiliated Hospital with Nanjing Medical University, Nanjing 210029, China. E-mail: yuansongtao@vip.sina.com.
- Q.H. Liu is with Department of Ophthalmology, The First Affiliated Hospital with Nanjing Medical University, Nanjing 210029, China. E-mail: liuqh@njmu.edu.cn.
- Q. Chen is with the School of Computer Science and Engineering, Nanjing University of Science and Technology, Nanjing 210094, China. E-mail: chen2qiang@njust.edu.cn.

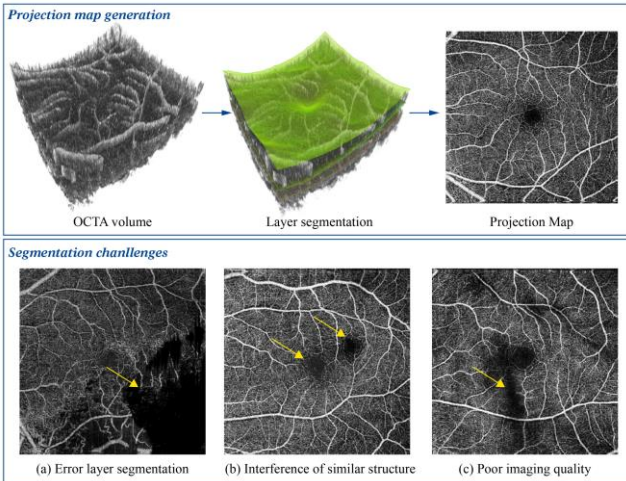


Fig. 1. The generation of projection map and the challenges in the RV segmentation and the FAZ segmentation.

In our previous work, we proposed an image projection network (IPN) [23], which can realize 3D-to-2D RV segmentation and FAZ segmentation. It uses the original 3D volumes as input instead of the projection maps, avoiding the use of retinal layer segmentation, thereby overcoming the negative effects of error layer segmentation. Besides, the use of volumetric information can help the network better distinguish the similar areas in the projection map, such as non-perfusion and FAZ area.

However, the IPN still has some limitations. For example, the lack of downsampling in the horizontal direction makes the IPN lack a wide range of receptive fields in the horizontal plane, which leads to the weak recognition ability in the horizontal direction. Besides, because the three-dimensional network will take up a lot of computing resources, in the case of limited computing resources, we need to cut the original data into small patches. In the process of splicing the segmentation results, we find that the segmentation results have a “checkerboard effect”.

To overcome the above limitations, in this work, we proposed image projection network-V2 (IPN-V2). IPN-V2 introduces a plane perceptron to strengthen the perceptron ability in the horizontal direction. Then, to overcome the “checkerboard effect” when splicing, we added a global re-training process in IPN-V2, dubbed IPN-V2+, which stitches the 2D feature maps output by the network, and then trains a global network. This process not only overcomes the “checkerboard effect”, but also provides the global information, which makes up for the limitations of patch training.

Moreover, in order to verify the effectiveness of our framework and to facilitate the research work of other researchers who focus on retinal image analysis, we released a well-organized multimodality dataset, dubbed OCTA-500. Our dataset contains OCT and OCTA volumes of two field of views (FOVs) from 500 subjects, including a total of more than 360k images, six types of projection maps, four types of text labels, and two types of pixel-level labels. The total size of the dataset is about 80GB. To our best knowledge, this is the largest OCTA public dataset so far. We perform a thorough evaluation of the performance of

IPN-V2 on the OCTA-500 dataset. The experimental results demonstrate that our IPN-V2 can achieve better performance than IPN and other 2D baselines.

This research followed the principles of the Declaration of Helsinki, and was approved by the institutional human Subjects Committee. All federal, state and local laws were abided by and this study was conducted with respect to all privacy regulations. Finally, our contributions include:

1) We proposed IPN-V2, which achieves better 3D-to-2D RV segmentation and FAZ segmentation. The code is publicly available at: https://github.com/chaosallen/IPNV2_pytorch.

2) We proposed OCTA-500, which is the largest OCTA dataset. The dataset is publicly available at: <https://iee-dataport.org/open-access/octa-500>.

2 RELATED WORKS

2.1 RV segmentation

The retinal vessel segmentation for fundus images has been studied for more than 20 years, and many methods have been accumulated in this field, such as: filtering-based methods [24], [25], [26], graph-based methods [27], [28], classifier-based methods [29], [30], and deep learning-based methods [31], [32], [33]. In contrast, OCTA imaging is a newly developed technology, and the practice of retinal vessel segmentation in OCTA images is relatively rare.

Gao et al. [34] quantified vessel density by a threshold-based method. Li et al. [6] applied the top-hat enhancement and optimally oriented flux algorithms to enhance and segment the vessels in the OCTA images. Eladawi et al. [7] proposed a joint Markov-Gibbs random field model to segment the retinal vessels in different projection maps. However, high signal in OCTA image may represent large blood vessels, capillaries and a lot of background noise, and it is difficult to distinguish them precisely using the above threshold-based and filtering-based methods. A modified U-Net was introduced by Pissas et al. [8] for vessel segmentation in OCT-A maximum intensity projection. Ma et al. [35] introduced a novel Split-based Coarse-to-Fine network with the ability to detect thick and thin vessels separately. The above methods mainly focus on the 2D projection images, which are obtained by the projection of OCTA volume under the limitation of retinal layer segmentation. Our previous work [23] proposed a novel 3D-to-2D image projection network to segment the 2D retinal vessels from 3D volume data.

2.2 FAZ segmentation

FAZ is a region of fovea without blood, whose area is related to the diabetic retinopathy [20] and the retinal vein occlusion [21]. Compared with retinal vessel segmentation, the FAZ segmentation in OCTA images is a relatively new study. Lu et al. [11] presented an active contour model to detect the FAZ. Díaz et al. [12] used a series of morphological operators to identify the FAZ candidates on OCTA projection images with two types of FOVs. Guo et al. [13] introduced a modified U-Net for the FAZ segmentation in

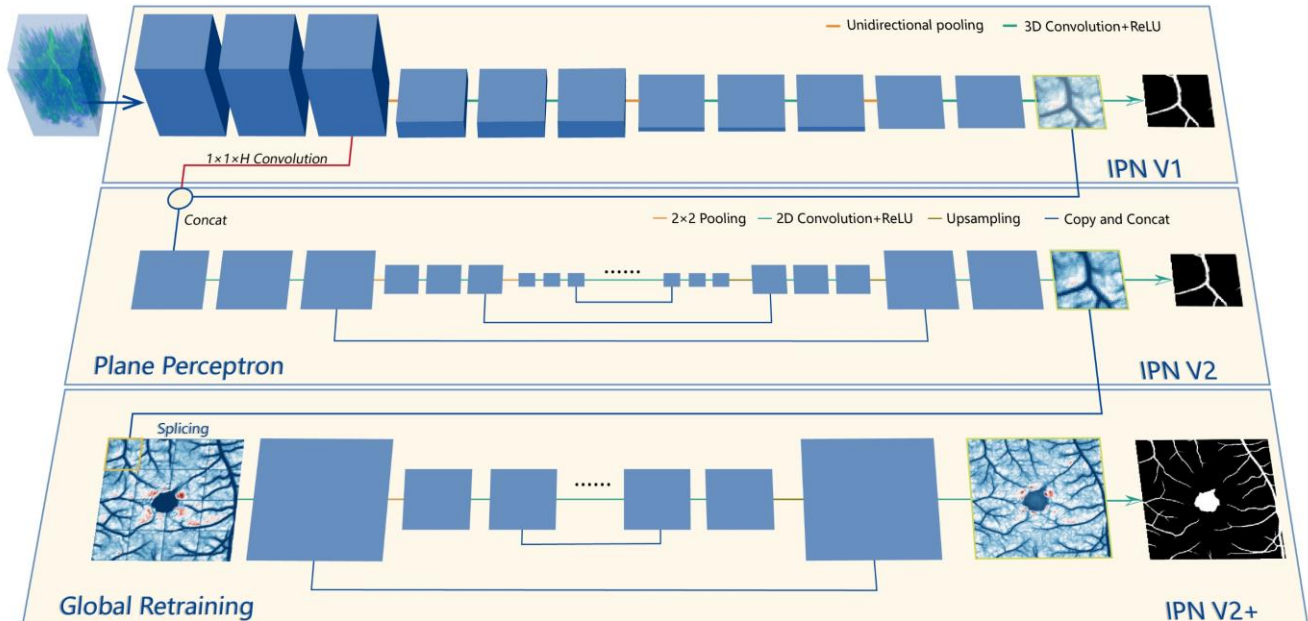


Fig. 2. The architecture of IPN V2 and IPN V2+.

the OCTA projection maps of the superficial retina. Guo et al. [14], [15] developed a CNN to segment the capillary nonperfusion area, which includes the FAZ region. In our previous work [10], a 2D U-shape network was used to segment the FAZ in OCT and OCTA projection maps for the fovea detection. We also used the proposed IPN [23] to segment the FAZ from 3D volume data.

2.3 OCTA Dataset

OCTA is a relatively new imaging modality with a late start. To our best knowledge, before we write this work, there is no publicly available OCTA database. A large OCTA database is urgently needed for researchers. Recently, a dataset named ROSE [35] for OCTA vessel segmentation is also ready to be released. Their database mainly contains 229 OCTA projection images with 3mm×3mm FOV and manual labels of vessels and capillaries. However, the corresponding 3D OCTA volumes are not released, which are also urgently needed by researchers, and we will discuss these needs in the Section 6. To motivate related studies for OCTA, we release the OCTA-500 dataset, which contains 3D volume data from 500 subjects. For more information, please refer to Section 4.

3 METHOD

In this section, we first review the design of the image projection network. Then we introduce our improvement proposals of IPN, including the IPN-V2 with the plane perceptron and the IPN-V2+ with the global retraining process. The proposed network architecture is shown in Fig. 2.

3.1 Image Projection Network

We proposed an image projection network in (Li et al., 2020) to achieve 3D-to-2D segmentation. The IPN f inputs the 3D volume $I^{L \times W \times H}$ and outputs the 2D segmentation result $O^{L \times W}$, denoted as:

$$I^{L \times W \times H} \xrightarrow{f} O^{L \times W} \quad (1)$$

The compression on scale H is achieved by introducing the unidirectional pooling, which only downsampling in the height direction. We design the projection learning modules composed of the convolution layer and the unidirectional pooling to gradually accumulate effective information from 3D space to a 2D plane, as shown in the first column of Fig. 2. IPN has been verified to be effective in the RV segmentation and the FAZ segmentation.

However, the IPN still has several limitations. For example, IPN uses the unidirectional pooling instead of traditional isotropic pooling. This change can maintain the scale of the network in the horizontal direction. Still, there is no downsampling operation in the horizontal direction, which makes the network lack high-level semantic information in the horizontal plane, and sometimes leads to the weak recognition ability of the network.

Besides, due to the large volume size and the limited computing resources, it is difficult to use the entire three-dimensional volume as the input of IPN in most cases. Specifically, when the batch size is set to 1, one 1080 Ti GPU is used, and the input size is 150*150*640 (about 1/8 of the 3D volume), the process is OOM. One solution is to reduce the size of original data, but downsampling will seriously affect the effect of segmentation. In particular, the width of most small retinal vessels is less than 5 pixels, and the structural information is lost severely after downsampling. Therefore, we adopted another strategy. We cut the original data $I^{L \times W \times H}$ into several patches $I^{l \times w \times h}$ as the input of IPN, and the output of network is $O^{l \times w}$. Then, we use a splicing algorithm s to obtain the final segmentation result $O^{L \times W}$. This practice is expressed as:

$$\begin{cases} I^{l \times w \times h} \xrightarrow{f} O^{l \times w}, I^{l \times w \times h} \subseteq I^{L \times W \times H} \\ O^{l \times w} \xrightarrow{s} O^{L \times W} \end{cases} \quad (2)$$

However, training patch by patch makes the network

lack global information; Besides, there is a “checkerboard” effect when splicing the segmentation results.

To solve these limitations, we introduce a plane perceptron module and a global retraining process on the basic structure of IPN.

3.2 Plane Perceptron

The main function of IPN is to summarize the 3D volume information into a 2D plane. Due to the lack of down-sampling in the horizontal direction, it lacks the high-level semantic information in the 2D plane. In IPN-V2, we propose a plane perceptron to make up for this deficiency.

The plane perceptron p is a 2D CNN structure connected behind the IPN. To strengthen the recognition of information in the 2D plane, the plane perceptron is used to reprocess the 2D features extracted by the IPN. In this work, we use U-Net [36] as a plane perceptron, due to its excellent two-dimensional segmentation ability. Besides, we concatenate the 2D features output by the IPN and the 3D features output by the first projection learning module to prevent the gradient from disappearing and speed up the convergence. The connection structure we adopt is $1 \times 1 \times H$ convolution with step size of H . The complete architecture of IPN-V2 is shown in the first two rows of Fig. 2 and expressed as:

$$\begin{cases} I^{l \times w \times H} \xrightarrow{f,p} O^{l \times w}, I^{l \times w \times H} \subseteq I^{L \times W \times H} \\ O^{l \times w} \xrightarrow{s} O^{L \times W} \end{cases} \quad (3)$$

3.3 Global Retraining

The plane perceptron improves the segmentation performance of the network, but the limitation of computing resources still exists. The input of IPN-V2 is only a small patch of the entire volume, and we need to adopt a splicing strategy to splice the outputs of the network.

First, we use a splicing method without overlap, and the segmentation result is misplaced at the splicing boundary. For the convenience of observation, we output the 2D feature maps from the network and use the same splicing strategy to splice them. The splicing result has a “checkerboard effect”, as shown in Fig. 3(a). It indicates that the network has a weak segmentation ability at the boundary. In our view, this is caused by the padding mechanism. To reduce this checkerboard effect, we have adopted a splicing method with overlap, as shown in Fig. 3(b), and the values in the overlapping areas are calculated based on the average value.

Although the splicing method with overlap reduces the checkerboard effect, it does not entirely overcome this effect. The degree of the checkerboard effect is related to the setting of the step d . The smaller the step, the weaker the checkerboard effect, but the time cost of the algorithm will increase. Besides, although we can obtain the final global segmentation result through splicing, due to segment patch by patch, the network does not make full use of global information.

To completely overcome the checkerboard effect and make the global information captured more by the network, we propose a global retraining process. We splice the 2D feature maps $O_m^{l \times w \times c}$ from the penultimate layer of IPN-V2 into a global feature map $O_m^{L \times W \times c}$, where c is the number

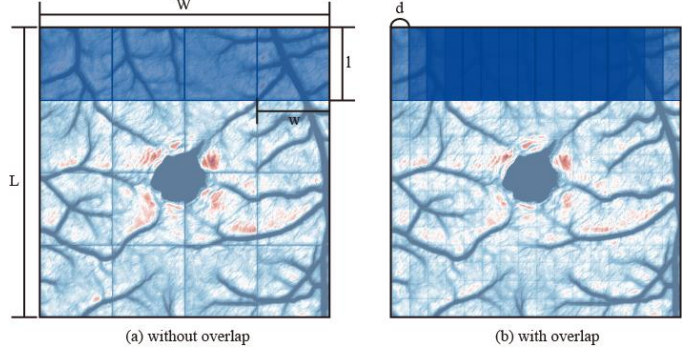


Fig. 3. Splicing methods without and with overlap.

of feature maps. Then, we input the global feature map $O_m^{L \times W \times c}$ into a global network g , using complete labels for supervision. In this work, the global network g is a U-shape network as shown in the third column of Fig. 2. Note that, the global network g is an additional training process. The training of global information in 3D volume requires too much computing resources, which determines that we use 2D features to capture global information, and also due to the limitation of computing resources, the plane perceptron p and the global network g cannot be combined. The output of the network g is the final global segmentation result $O_n^{L \times W}$. We name the entire segmentation process as IPN-V2+, and this process can be expressed as:

$$\begin{cases} I^{l \times w \times H} \xrightarrow{f,p} O^{l \times w \times c}, I^{l \times w \times H} \subseteq I^{L \times W \times H} \\ O_m^{l \times w \times c} \xrightarrow{s} O_m^{L \times W \times c}, O_m^{L \times W \times c} \xrightarrow{g} O_n^{L \times W} \end{cases} \quad (4)$$

Specifically, IPN-V2+ needs to train two networks. We first train the IPN-V2 to get the feature maps, which is then fed into the global network to perform global retraining. Notably, due to the different functions undertaken by the two networks, the training phase can be completed on one training set.

4 DATASET

In this section, we introduce our proposed dataset OCTA-500. OCTA-500 is a multi-modality dataset collected from 500 subjects with two field of view (FOV) types. The dataset includes two modality types of volumes, six types of projections, four types of text labels and two types of pixel level labels. The dataset contains more than 360K images with a size of about 80GB. The structure of OCTA-500 is shown in Fig. 4.

4.1 Data Sources

OCTA-500 contains two subsets, which is divided according to the FOV type. One subset contains 300 subjects with $6\text{mm} \times 6\text{mm}$ FOV, named OCTA_6M. Another subset contains 200 subjects with $3\text{mm} \times 3\text{mm}$ FOV, named OCTA_3M. The data were collected using a commercial 70 kHz spectral-domain OCT system with a center wavelength of 840 nm (RTVue-XR, Optovue, CA). OCTA_6M are collected from the subjects imaged from Jiangsu Province Hospital between March 2018 to September 2019. Only one imaging for one eye of each subject is included, which ensures diversity and avoids similar data. OCTA_3M comes from an independent collection, mainly

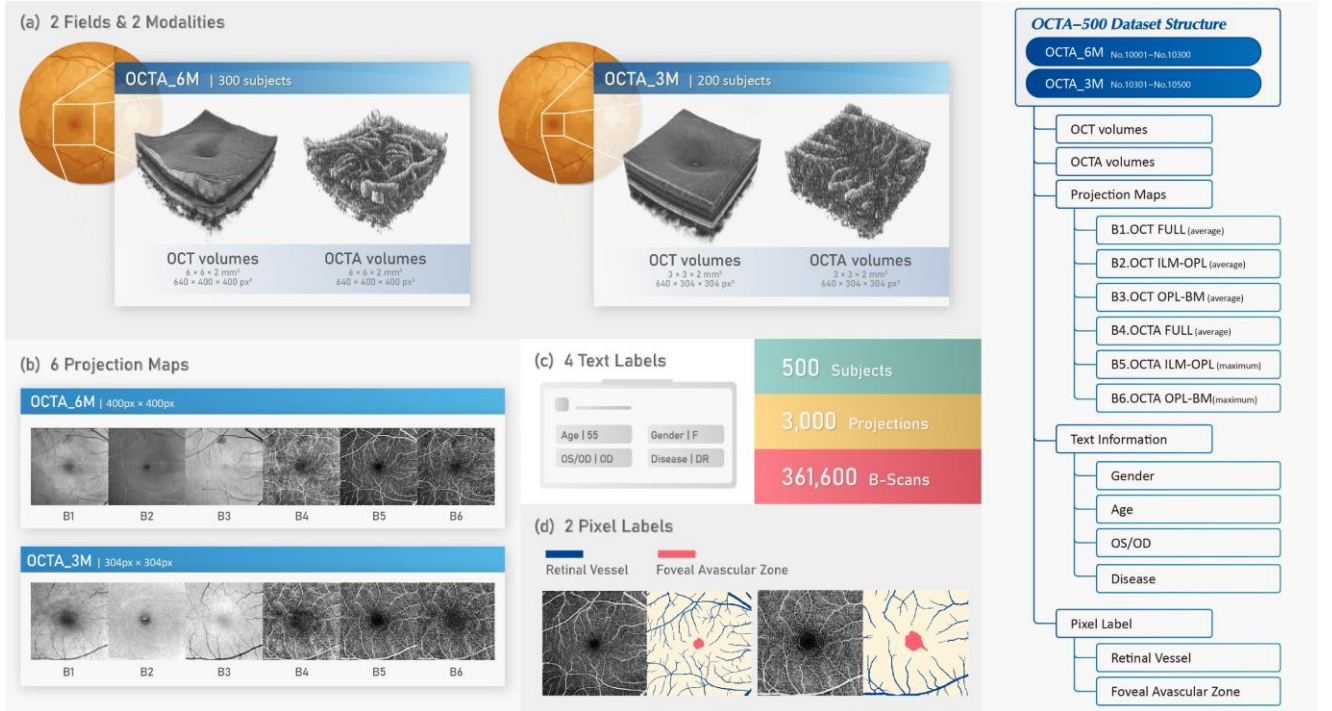


Fig. 4. The proposed OCTA-500 dataset.

from the normal population, and the diseased population only including AMD, DR, and CNV. The registration information of all subjects is complete, and the type of diagnosed disease is given by ophthalmologists.

We used the Iowa software (OCTExplorer 3.8) [37], [38], [39] and the layer segmentation method [40] to segment three retinal layers in 500 OCT volumes, and manually select better segmentation results. The layer segmentation is used to generate six kinds of projection maps, as supplementary research objects. In addition, in order to obtain the distribution of data, we queried the medical records of these subjects and collated four types of text labels, which were also included in the dataset. Finally, we draw the ground truth of the RV segmentation and FAZ segmentation for training and evaluation of our proposed IPN-V2. The structures of the OCT and OCTA volumes are introduced in Sec. 4.2. The generation of projection maps is illustrated in Sec. 4.3. The text labels and data distribution will be given in Sec. 4.4. The pixel labels for two segmentation tasks and its drawing guidelines will be explained in Sec. 4.5.

4.2 OCT and OCTA Volumes

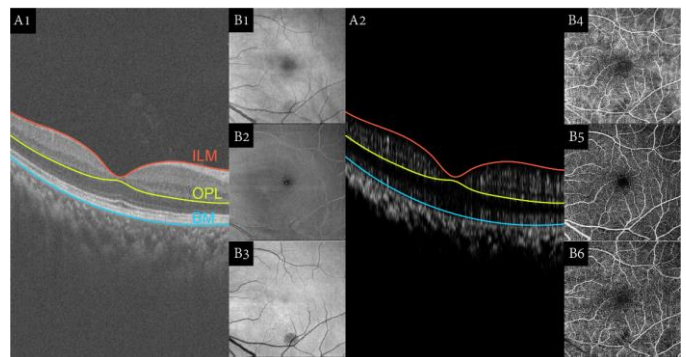
OCTA-500 dataset contains volume data of two modalities, OCT and OCTA volumes. OCT volumes and OCTA volumes provide structural information and blood flow information of the retina, respectively. OCTA volume is generated from the OCT volume by the split-spectrum amplitude-decorrelation angiography (SSADA) algorithm [41]. Due to the use of band-pass filtering and split-spectrum methods in SSADA algorithm, the vertical resolution of the OCTA volume is 1/4 of the OCT volume. We use bilinear interpolation to resize it, and then the OCT and OCTA volumes are perfectly registered.

OCTA-500 dataset contains two subsets, OCTA_6M and

OCTA_3M. The FOV of the two subsets is different, and their resolution are also inconsistent. OCTA_6M contains 300 subjects (NO.10001-NO.10300), whose imaging range is $6\text{mm} \times 6\text{mm} \times 2\text{mm}$ centered on the fovea, and the volume size is $400\text{px} \times 400\text{px} \times 640\text{px}$. OCTA_3M contains 200 subjects (NO.10301-NO.10500), whose imaging range is $3\text{mm} \times 3\text{mm} \times 2\text{mm}$ centered on the fovea, and the volume size is $304\text{px} \times 304\text{px} \times 640\text{px}$.

4.3 Projection Maps

We provide six types of projection images, as shown in Fig. 5. We first segment three retinal layers, which are internal limiting membrane (ILM) layer, outer plexiform layer (OPL), and Bruch's membrane (BM). Then two kinds of projection methods are selected for the generation of projection maps: average projection and maximum projection.



NUMBER	B1	B2	B3	B4	B5	B6
MODALITY	OCT	OCT	OCT	OCTA	OCTA	OCTA
REGION	FULL	ILM-OPL	OPL-BM	FULL	ILM-OPL	OPL-BM
MODE	Average	Average	Average	Average	Maximum	Maximum

Fig. 5. Generation of projection maps. (A1) OCT B-scan. (A2) OCTA B-scan. (B1-B3) OCT projection images. (B4-B6) OCTA projection images. The table lists the modality, projection region and projection mode of each projection image.

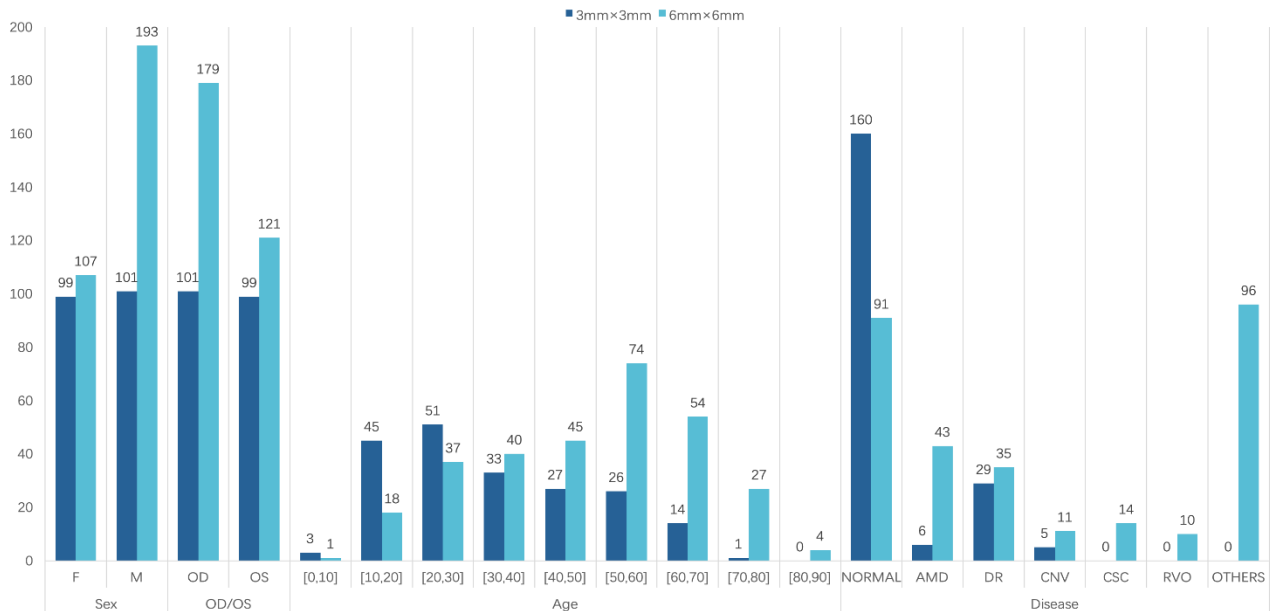


Fig. 6. Data distribution of different text labels in OCTA-500.

They are obtained by averaging or maximum along the axial direction. The OCT volume usually uses the average projection. Since the value in OCTA volume reflects the intensity of the blood flow signal, in order to show the shape of blood vessels more clearly, the maximum projection is usually used in the projection images of inner retina and outer retina. The six types of projection map we generated are as follows:

1) OCT full-projection (B1). It is the average value of 3D OCTA volume along the axial direction, which shows the global information of OCTA volume, mainly including retina and choroid.

2) OCT average-projection between ILM and OPL (B2). It can show the vessels in the inner retina with high reflection [42].

3) OCT average-projection between OPL and BM (B3). It displays the vessel shadows in the outer retina with low reflection. Both projection image B2 and projection image B3 are critical views of vascular morphology in OCT volume [42].

4) OCTA full-projection (B4). It is the average value of 3D OCTA volume along the axial direction, which is a view of both retina and choroid.

5) OCTA maximum-projection between ILM and OPL (B5). It is generated by the maximum projection of the inner retina which can clearly show the vascular morphology of the inner retina and the shape of the FAZ [11]. This is the most commonly used OCTA projection map, usually used for the RV segmentation and the FAZ segmentation [6], [7], [8], [10], [11], [12], [13], [14], [15].

6) OCTA maximum-projection between OPL and BM (B6). It is generated by the maximum projection of the outer retina, and it mainly contains the artifacts of large vessels and CNV. After removing the artifacts, it can be used to observe and monitor the morphology of CNV [16].

4.4 Text Labels

We queried the medical records of the 500 subjects. After desensitization, we collated four types of text labels as follow: 1) Gender; 2) OS/OD; 3) Age; 4) Disease. The distribution of the text labels is shown in Fig. 6. The average ages of subjects included in the OCTA_6M and OCTA_3M are 49.18 ± 17.28 and 33.12 ± 16.17 , respectively. The proportion of subjects with ophthalmic diseases in OCTA_6M is 69.7%, while the proportion of subjects with ophthalmic diseases in OCTA_3M is 20%. The diseases mainly include age-related macular degeneration (AMD), diabetic retinopathy (DR), choroidal neovascularization (CNV), central serous chorioretinopathy (CSC) and retinal vein occlusion (RVO). There are two cases where subjects are classified into the ‘others’ category. One situation is that there are few subjects with the disease, and another situation is that there are few subjects with the disease. These few diseases include retinal detachment (RD), retinal hemorrhage (RH), optic atrophy (OA),

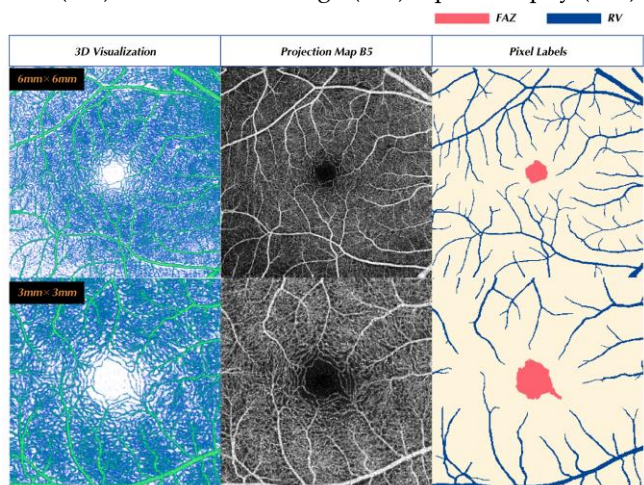


Fig. 7. Ground truth of the retinal vessel and the foveal avascular zone.

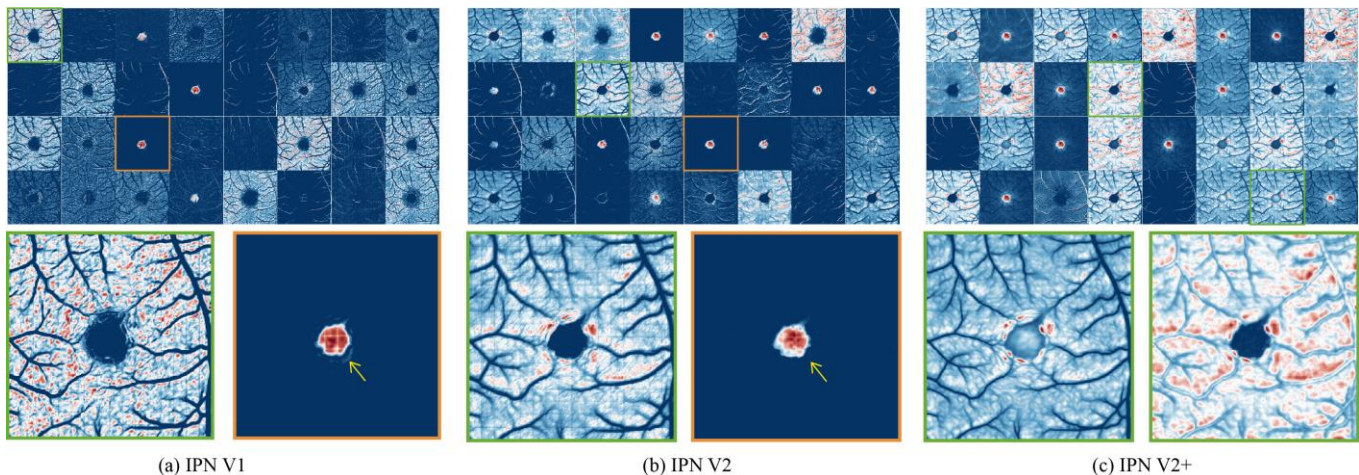


Fig. 8. The feature maps obtained by the IPN, IPN-V2 and IPN-V2+ in the segmentation of RV and FAZ.

epiretinal membrane (ERM), retinitis pigmentosa (RP), central retinal artery occlusion (CRAO), retinoschisis and so on.

4.5 Pixel Labels

In order to evaluate the performance of IPN-V2, we draw two types of pixel labels as follows:

1) RV Segmentation

Retinal vessel segmentation is of great significance in retinal disease analysis [43]. The blood flow information in OCTA images includes large blood vessels and capillaries. The segmentation of capillaries often needs to remove the mask of the large blood vessels in the projection images [6]. Their large vessel mask is generated by thresholding filtered image, which is relatively simple but difficult to segment large retinal vessels accurately. In this work, we carefully draw the large retinal vessels to assist in the research of vessel segmentation in OCTA images.

We draw the pixel labels of RV segmentation in the projection map B5, which can present clear large blood vessels in the inner retina. The blood vessels we draw do not include capillary plexus, and some small vessel plexus with ambiguous definitions are excluded. The blood vessel plexus around the FAZ is not within the definition of large vessels. Five trained researchers draw the ground truth, and three ophthalmologists review the drawing results. After modification, this laborious work was completed. The blue color in Fig. 7 represents the ground truth of the RV in the two subsets.

2) FAZ Segmentation

OCTA can clearly show the outline of the foveal avascular zone. A large number of studies have focused on the differences of FAZ in different populations [20], [21], and the automatic FAZ segmentation in OCTA has become necessary research. In this work, we draw the ground truth of the FAZ region to assist in the research of FAZ segmentation in OCTA images.

The ground truth for FAZ segmentation is also drawn in the projection map B5. The FAZ is drawn based on the largest closed-loop surrounded by a capillary network in the central recess of the macula. As a principle, the boundary of the FAZ is as close as possible to the surrounding capillary plexus, and the region of FAZ should contain as

little high-intensity signals as possible. One expert drew the ground truth, and two ophthalmologists revised the drawing results. The red color in Fig. 7 shows the ground truth of the FAZ in the two subsets.

5 EXPERIMENT

We evaluated the segmentation performance of IPN-V2 and IPN-V2+ on the OCTA-500 dataset, and performed quantitative and qualitative comparisons with the baseline methods.

5.1 Baseline Methods

We compared our method with other state-of-the-art segmentation methods, including 3D-to-2D method IPN [23] and six 2D-to-2D deep learning approaches: Fast-FCN [44], Deeplab V3+ [45], Attention U-Net [46], U-Net [36], U-Net 2+ [47], U-Net 3+ [48]. We fine-tuned the structure of Fast-FCN and Deeplab V3+. Specifically, we connected the last upsampling layer with the first convolution layer of the networks and added two convolutional layers to restore the output size to the original image size. The structural parameters (such as the number of channels, the number of convolutional layers) in baseline networks were manually adjusted to yield the best achievable performances.

For each baseline network and our proposed method, RV segmentation and FAZ segmentation are implemented separately. Since the relationship between the RV and the FAZ may improve the segmentation performance, to explore the impact of multi-task learning on network performance, we used the multi-class cross-entropy loss in several baseline networks to simultaneously segment the RV and the FAZ.

5.2 Experimental Setting

We set the experiments on two subsets of OCTA-500. OCTA_6M is divided into a training set (NO.10001-NO.10180), a validation set (NO.10181-NO.10200), a test set (NO.10201-NO.10300). OCTA_3M is divided into a training set (NO.10301-NO.10440), a validation set (NO.10441-NO.10450), a test set (NO.10451-NO.10500). We use the training set to train network parameters, use the validation set to select the best model and the best threshold, and use the test set for evaluation. Specially, each group of experiments was

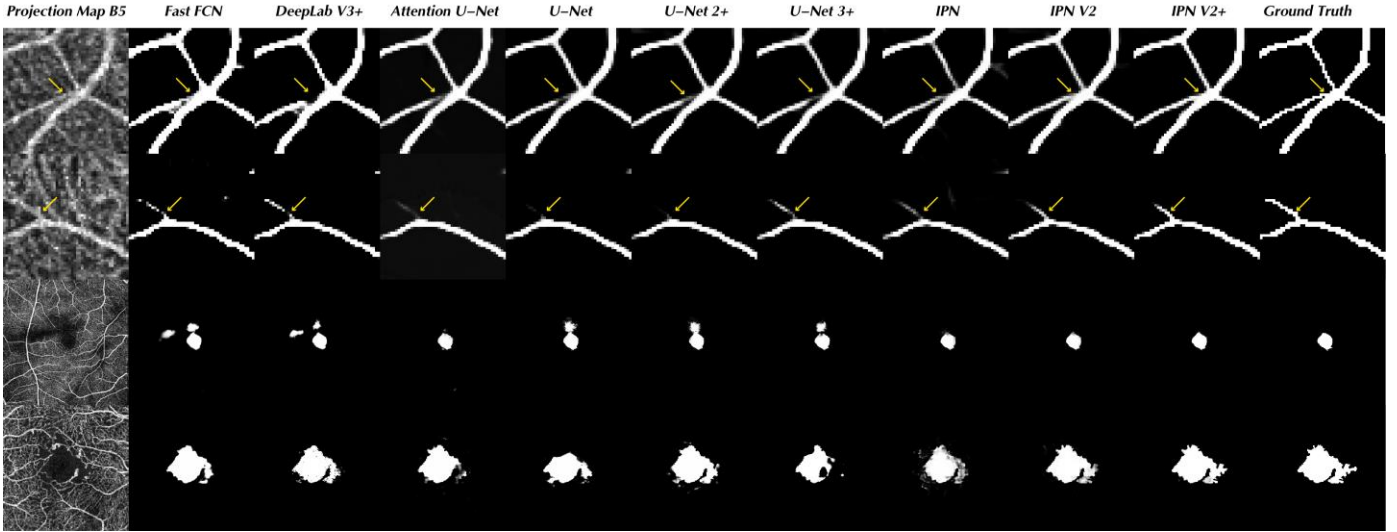


Fig. 9. Comparison of the segmentation results from different methods. The first two rows compare the local results of the RV segmentation, and the last two rows compare the segmentation results of the FAZ.

implemented three times and selected the model with the highest Dice score on the validation set as the final model to evaluate the test set.

The proposed methods and baselines are all implemented with PyTorch on 1 NVIDIA GeForce GTX 1080Ti GPU. Due to the different characteristics of these methods, we divide them into two cases with different experimental settings: 2D-to-2D methods and 3D-to-2D methods.

2D-to-2D methods. The input of 2D-to-2D methods like U-Net is the projection image B5 on which we draw the ground truth. We use cross-entropy loss function and train the network using Adam optimization with a batch size of 4 and an initial learning rate of 0.0001. The maximum number of iterations is 10000. The frequency of model saving is per 200 iterations.

3D-to-2D methods. We use OCT and OCTA volumes as the input of 3D-to-2D methods. In FAZ segmentation, we use the distance map introduced in [23] as an additional input. The volume size in OCTA_6M is $400 \times 400 \times 640$, and the patch size is $100 \times 100 \times 160$; The volume size in OCTA_3M is $304 \times 304 \times 640$, and the patch size is $76 \times 76 \times 160$. We performed blocking in the first two dimensions and the bilinear interpolation in the third dimension. We train the IPN-V2 using Adam optimization with a batch size of 1 and an initial learning rate of 0.0001. The maximum number of iterations is 30000. The frequency of model saving is per 500 iterations. We train the global retraining network in IPN-V2+ using Adam optimization with a batch size of 2 and an initial learning rate of 0.0001. The maximum number of iterations is 5000. The frequency of model saving is per 50 iterations.

5.3 Evaluation Metrics

We used three metrics to evaluate the segmentation results objectively:

- 1) Dice coefficient (DICE): $2TP/(2TP+FP+FN)$;
- 2) Jaccard index (JAC): $TP/(TP+FP+FN)$;
- 3) Balance accuracy (BAC): $(TPR+TNR)/2$;

where TP is true positive, FP is false positive, FN is false negative, TPR is true positive rate, and TNR is true negative rate. The Dice coefficient and the Jaccard index are the two most representative commonly used evaluation metrics for image

segmentation. Besides, since the pixels of negative samples are much more than that of positive samples in the two tasks, we use the balanced accuracy instead of accuracy to prevent over-evaluation.

5.4 Performance Comparison and Analysis

We make a quantitative and qualitative comparison and analysis of the segmentation results of the proposed network and the baseline networks on the two subsets of OCTA-500 dataset. Table I and Table II list the objective evaluation results of the RV segmentation and the FAZ segmentation, respectively.

Performance on multi-task learning. We conducted multi-task learning experiments on several networks, that is, RV and FAZ were simultaneously segmented. We hope that RV segmentation can provide a position reference to facilitate FAZ segmentation. However, we have not found a significant improvement in the results of the multi-task learning and even the segmentation performance decreased in some experiments. On the one hand, the distribution of the RV in the OCTA image is obvious and can be easily discovered by network. Thus, the promotion of the RV segmentation on the FAZ segmentation is limited. On the other hand, it is difficult to guarantee that the same model can achieve the best performance on the FAZ and RV segmentation at the same time.

Ablation of IPN, IPN-V2, and IPN-V2+. We conducted ablation studies on IPN, IPN-V2, and IPN-V2+ to explore the impact of our proposed plane perceptron and global retraining process on segmentation performance. As shown in Table I and Table II, the quantitative results of IPN-V2 in all task are better than IPN. The Dice, Jaccard and balance accuracy are averagely increased by 1.8%/2.9%/1% respectively. As shown by the yellow arrow in Fig. 8, there are several falsely segmented areas around FAZ in the feature map from IPN, and IPN-V2 excludes these areas, which reflects that IPN-V2 has a better recognition ability than IPN in the horizontal direction. The above evidence proves that the introduction of the plane perceptron in IPN-V2 is an effective strategy. Besides, the results of IPN-V2+ are also better than IPN-V2 with an increase of about 0.25%/0.44% in Dice and Jaccard. As shown by the green box in Fig. 8, the feature maps of IPN and IPN V2 both have the "checkerboard effect", while it is not obvious in the

TABLE 1
QUANTITATIVE COMPARISON OF RETINAL VESSEL SEGMENTATION ON OCTA-500 DATASET (MEAN \pm SD)

P* REPRESENTS PLANE PERCEPTRON. G* REPRESENTS GLOBAL RETRAINING. M* REPRESENTS MULTITASK LEARNING.

RV Segmentation				OCTA_6M (6mm \times 6mm)			OCTA_3M (3mm \times 3mm)		
Methods	P*	G*	M*	DICE (%)	JAC (%)	BACC (%)	DICE (%)	JAC (%)	BACC (%)
2D to 2D									
Fast-FCN [44]	-	-	-	86.59 \pm 3.22	76.49 \pm 4.70	92.00 \pm 1.88	88.45 \pm 2.42	79.38 \pm 3.75	93.62 \pm 1.28
DeepLab V3+ [45]	-	-	-	87.22 \pm 3.14	77.47 \pm 4.63	92.81 \pm 1.69	88.02 \pm 2.48	78.69 \pm 3.82	92.71 \pm 1.51
Attention U-Net [46]	-	-	-	88.67 \pm 2.76	79.75 \pm 4.23	93.36 \pm 1.62	90.89 \pm 2.21	83.38 \pm 3.56	94.71 \pm 1.62
U-Net [36]	-	-	-	88.28 \pm 2.59	79.11 \pm 3.97	92.98 \pm 1.62	90.60 \pm 2.16	82.88 \pm 3.47	94.91 \pm 1.38
U-Net [36]	-	-	✓	88.44 \pm 2.58	79.37 \pm 3.99	92.94 \pm 1.59	90.19 \pm 2.21	82.20 \pm 3.54	94.23 \pm 1.46
U-Net 2+ [47]	-	-	-	88.62 \pm 2.61	79.66 \pm 4.02	93.30 \pm 1.53	90.84 \pm 2.20	83.29 \pm 3.55	94.96 \pm 1.45
U-Net 2+ [47]	-	-	✓	88.15 \pm 2.93	78.92 \pm 4.40	92.86 \pm 1.74	90.31 \pm 2.23	82.40 \pm 3.58	94.39 \pm 1.48
U-Net 3+ [48]	-	-	-	88.49 \pm 2.80	79.47 \pm 4.26	93.07 \pm 1.78	90.92 \pm 2.08	83.41 \pm 3.36	94.57 \pm 1.43
U-Net 3+ [48]	-	-	✓	88.78 \pm 2.63	79.92 \pm 4.07	93.37 \pm 1.57	90.93 \pm 2.05	83.43 \pm 3.35	95.12 \pm 1.40
3D to 2D									
IPN [23]	-	-	-	88.64 \pm 3.21	79.73 \pm 4.92	93.07 \pm 2.42	90.62 \pm 5.96	83.25 \pm 7.78	93.87 \pm 4.19
IPN [23]	-	-	✓	88.30 \pm 3.36	79.21 \pm 5.11	92.79 \pm 2.55	91.10 \pm 3.49	83.83 \pm 5.29	94.63 \pm 2.79
IPN V2	✓	-	-	89.08 \pm 2.73	80.41 \pm 4.29	93.52 \pm 2.13	92.46 \pm 3.93	86.19 \pm 5.83	95.34 \pm 3.16
IPN V2	✓	-	✓	88.78 \pm 3.21	79.96 \pm 4.89	93.40 \pm 2.16	92.32 \pm 3.59	85.91 \pm 5.44	95.05 \pm 3.03
IPN V2+	✓	✓	-	89.41 \pm 2.74	80.95 \pm 4.32	93.46 \pm 2.12	92.74 \pm 3.95	86.67 \pm 5.88	95.22 \pm 3.12
IPN V2+	✓	✓	✓	89.18 \pm 3.15	80.61 \pm 4.84	93.37 \pm 2.16	92.63 \pm 3.43	86.44 \pm 5.25	95.20 \pm 2.90

TABLE 2
QUANTITATIVE COMPARISON OF FOVEAL AVASCULAR ZONE SEGMENTATION ON OCTA-500 DATASET (MEAN \pm SD)

P* REPRESENTS PLANE PERCEPTRON. G* REPRESENTS GLOBAL RETRAINING. M* REPRESENTS MULTITASK LEARNING.

FAZ Segmentation				OCTA_6M (6mm \times 6mm)			OCTA_3M (3mm \times 3mm)		
Methods	P*	G*	M*	DICE (%)	JAC (%)	BACC (%)	DICE (%)	JAC (%)	BACC (%)
2D to 2D									
Fast-FCN [44]	-	-	-	86.01 \pm 15.62	77.84 \pm 17.96	93.89 \pm 7.86	95.55 \pm 6.39	92.03 \pm 9.24	98.10 \pm 1.47
DeepLab V3+ [45]	-	-	-	87.20 \pm 14.94	79.50 \pm 17.10	94.15 \pm 7.84	96.60 \pm 3.19	93.60 \pm 5.56	98.56 \pm 1.23
Attention U-Net [46]	-	-	-	88.97 \pm 14.02	82.26 \pm 17.43	95.23 \pm 7.65	97.11 \pm 2.03	94.46 \pm 3.73	99.09 \pm 1.20
U-Net [36]	-	-	-	88.10 \pm 17.56	81.78 \pm 19.99	94.29 \pm 9.29	96.81 \pm 2.96	93.97 \pm 5.14	98.69 \pm 2.09
U-Net [36]	-	-	✓	88.12 \pm 13.60	80.73 \pm 16.53	94.42 \pm 7.64	96.57 \pm 2.24	93.46 \pm 4.06	98.61 \pm 1.54
U-Net 2+ [47]	-	-	-	87.79 \pm 18.00	81.32 \pm 19.76	94.39 \pm 9.63	97.10 \pm 2.10	94.44 \pm 3.89	98.85 \pm 1.16
U-Net 2+ [47]	-	-	✓	87.08 \pm 16.95	79.89 \pm 19.06	94.03 \pm 8.96	96.82 \pm 1.83	93.89 \pm 3.36	98.80 \pm 1.07
U-Net 3+ [48]	-	-	-	88.15 \pm 16.68	81.67 \pm 19.70	94.68 \pm 9.02	97.45 \pm 1.72	95.09 \pm 3.20	99.11 \pm 1.12
U-Net 3+ [48]	-	-	✓	87.27 \pm 16.02	80.07 \pm 19.26	93.57 \pm 8.75	97.26 \pm 1.57	94.72 \pm 2.92	98.71 \pm 1.15
3D to 2D									
IPN [23]	-	-	-	88.02 \pm 9.91	79.80 \pm 13.81	95.44 \pm 4.63	95.05 \pm 4.79	90.91 \pm 7.98	97.68 \pm 3.21
IPN [23]	-	-	✓	87.65 \pm 11.48	79.52 \pm 15.10	93.57 \pm 6.93	95.08 \pm 5.84	91.13 \pm 9.34	97.27 \pm 4.35
IPN V2	✓	-	-	90.68 \pm 8.87	83.97 \pm 12.64	96.42 \pm 4.24	97.30 \pm 2.33	94.84 \pm 4.15	98.83 \pm 1.64
IPN V2	✓	-	✓	90.42 \pm 10.32	83.88 \pm 14.60	96.07 \pm 4.83	97.36 \pm 2.17	94.93 \pm 3.92	98.63 \pm 1.75
IPN V2+	✓	✓	-	90.84 \pm 8.93	84.23 \pm 12.69	96.37 \pm 4.08	97.55 \pm 2.38	95.32 \pm 4.19	98.74 \pm 1.74
IPN V2+	✓	✓	✓	90.54 \pm 10.05	84.00 \pm 14.16	96.67 \pm 4.29	97.42 \pm 2.16	95.04 \pm 3.88	98.55 \pm 1.75

feature maps of IPN-V2+. It indicates that the global retraining process in IPN-V2+ can effectively overcome the "chessboard effect". In summary, our improvements in IPN-V2 and IPN-V2+ are effective, and IPN-V2+ has achieved the best performance in all tasks.

Comparison on RV segmentation. The quantitative comparison of the RV segmentation is shown in Table I. U-Net 3+ achieves the best Dice and Jaccard in the 2D-to-2D methods, and IPN-V2+ can achieve the best Dice and Jaccard in the 3D-to-2D methods. The Dice and Jaccard of IPN-V2+ are 1.2%/2.1% higher than U-Net 3+, respectively. Fig. 9 compares the probability maps of the results of two typical RV segmentation examples. The yellow arrows in Fig. 9 show that the

completeness and connectivity of the RV segmentation in the 3D-to-2D methods perform better than that in the 2D-to-2D methods. In our analysis, segmentation in the 2D projection map is more susceptible to noise interference, and the 3D volumes provide more structural information to improve the performance of RV segmentation. Besides, it is easy to find that the performance of IPN-V2 and IPN-V2+ are better than IPN in the RV segmentation, and the proposed IPN-V2+ achieves state-of-the-art RV segmentation performance.

Comparison on FAZ segmentation. The quantitative comparison of the FAZ segmentation is shown in Table II. Because the OCTA_6M subset contains a variety of diseases, as shown in Fig. 6, while normal subjects account for the

majority in OCTA_3M subset, segmentation in the OCTA_6M is more challenging than that in the OCTA_3M. In OCTA_6M, Attention U-Net achieves the best FAZ segmentation in the 2D-to-2D methods. The third row of Fig. 9 indicates that the attention mechanism might help the U-Net focus on the FAZ area, avoiding the interference of similar areas to a certain extent. IPN V2+ achieves the best Dice and Jaccard in the 3D-to-2D methods. The Dice and Jaccard of IPN-V2+ are 1.9%/2.0% higher than those of Attention U-Net respectively. Fig. 9 lists two samples of FAZ segmentation with challenging. In the first sample, most of the 2D-to-2D methods (except Attention U-Net) have incorrectly identified some areas, which have weak signal and are similar to the FAZ area, while all 3D methods segmented well in this sample. It indicates that some additional information provided by the 3D volume, such as the retina thickness, helps the network reduce its dependence on the signal strength in the FAZ segmentation. In the second sample, the FAZ has a complex shape, and only the segmentation results of Deeplab V3+, U-Net 2+, IPN-V2 and IPN-V2+ are relatively complete, but the segmentation results of Deeplab V3+ and U-Net 2+ contain more noise. The segmentation result of the proposed IPN-V2+ is the best. Combined with the quantitative results, we can conclude that the proposed IPN-V2.

6 DISCUSSION

In addition to the aforementioned RV segmentation and FAZ segmentation, the large amount of data information contained in OCTA-500 may have many extensive applications. We will discuss several potential applications as follows:

6.1 Modality Transformation

OCT provides structural information of the retina, while OCTA displays the blood flow information. In fact, the OCTA volume is obtained from the continuous-time OCT images through the SSADA algorithm, so OCTA and OCT image are naturally and strictly registered. Lee et al. [49] considered OCTA images as the ground truth and used a deep learning method to generate blood flow signals from OCT images. Transforming from OCT to OCTA is a valuable study because the current cost of OCTA equipment is expensive. Our database contains three-dimensional volume data of OCT and OCTA, which can support the research on the modality transformation.

6.2 Disease Diagnosis

In OCTA-500 dataset, we provide multiple disease labels, which can be used as the design of disease classification algorithms. Kermany et al. [50] used a transfer learning method to train models in more than 100,000 OCT B-scans to classify diseases into four categories: CNV, diabetic macular edema (DME), Drusen, and normal case. Our database contains not only a large number of OCT B-scan images, but also their corresponding OCTA B-scan images, which may help promote classification accuracy for diseases such as DR. The projection images we provide can also be used as a modality consideration to improve the performance of disease classification. In addition, other text labels, such as age, can be used to assist AMD diagnosis. We hope that these different modality data and text labels can provide

more ideas in disease diagnosis for researchers.

6.3 Multi-modality Fusion and Visualization

We generated six types of projection images that contained information on different retinal layers. These projection images have their own characteristics. For example, the B1 projection can show the area of retinal edema, the B3 projection images can show artifacts of large blood vessels and have a cleaner field of view, the B5 projection images can clearly show the large blood vessels and capillary plexus of the inner retina, and the B6 projection images can show the shape of CNV. It can be considered that fusion their own useful information to generate new views for doctors to observe and diagnose diseases. For example, Jia et al. [16] detected the CNV area in the B6 projection images and merged it into the B5 projection to improve the readability of the CNV in the OCTA projection. More useful visualization solutions are expected.

6.4 Quantification of Blood Flow Indicator

Several methods for quantifying blood flow have been proposed, such as vessel density (VD) [34], vessel diameter index (VDI) [51] and vessel tortuosity (VT) [52], etc. Recent research has been proposed by Romo et al. [53], which combines the FAZ segmentation and RV segmentation to estimate the blood flow density in the projection images. We have discussed the precise segmentation of large blood vessels and FAZ in this paper, which will help the further implementation of this work. Besides, the quantification of blood flow density also needs the support of the artifact removal algorithms [54], [55], [56], [57], and our database provides labels for large blood vessels, which have potential value for the removal of artifacts and the quantitative analysis of current artifact removal methods. In the future, better artifact removal methods and more useful blood flow schemes are expected to be verified in our database.

7 CONCLUSION

In this work, we present the IPN-V2 (and IPN-V2+) for the RV segmentation and the FAZ segmentation. We also propose the OCTA-500 dataset, which contains 500 subjects with two FOV types, including OCT and OCTA volumes, six types of projections, four types of text labels, and two types of pixel-level labels. To the best of our knowledge, this is the largest publicly available OCTA database until now. We perform a comprehensive evaluation for IPN-V2 on the two subsets of the OCTA-500. The experimental results demonstrate that our proposed IPN-V2 and IPN-V2+ perform better than IPN and other deep learning methods in the segmentation tasks. Finally, we discussed some potential applications of the OCTA-500 database in OCTA image analysis. Hopefully, our method and dataset will stimulate more research interest.

ACKNOWLEDGMENT

This study was supported by National Natural Science Foundation of China (61671242, 61701192), Key R&D Program of Jiangsu Science and Technology Department (BE2018131).

REFERENCES

- [1] D. Huang, E. A. Swanson, C. P. Lin, J. S. Schuman, W. G. Stinson, W. Chang, et al., "Optical coherence tomography," *Science*, vol. 254, no. 5035, pp. 1178–1181, 1991.
- [2] A. H. Kashani, C. Chen, J. K. Gahm, F. Zheng, G. M. Richter, P. J. Rosenfeld, et al., "Optical coherence tomography angiography: A comprehensive review of current methods and clinical applications," *Progress in Retinal and Eye Research*, vol. 60, pp. 66–100, 2017.
- [3] A. Zhang, Q. Zhang, C. Chen, and R. K. Wang, "Methods and algorithms for optical coherence tomography-based angiography: a review and comparison," *Journal of Biomedical Optics*, vol. 20, no. 10, 2015.
- [4] R. F. Spaide, J. G. Fujimoto, N. K. Waheed, S. R. Sadda, and G. Staurengi, "Optical coherence tomography angiography," *Progress in Retinal and Eye Research*, vol. 64, pp. 1–55, 2018.
- [5] T. E. D. Carlo, A. Romano, N. K. Waheed, and J. S. Duker, "A review of optical coherence tomography angiography (OCTA)," *International Journal of Retina and Vitreous*, pp. 1–5, 2015.
- [6] A. Li, J. You, C. Du, and Y. Pan, "Automated segmentation and quantification of OCT angiography for tracking angiogenesis progression," *Biomedical Optics Express*, vol. 8, no. 12, pp. 5604–5616, 2017.
- [7] N. Eladawi, M. Elmogy, O. Helmy, A. Aboelfetouh, A. Riad, H. Sandhu, et al., "Automatic blood vessels segmentation based on different retinal maps from OCTA scans," *Computers in Biology and Medicine*, vol. 89, pp. 150–161, 2017.
- [8] T. Pissas, E. Bloch, M. J. Cardoso, B. Flores, O. Georgiadis, S. Jalali, et al., "Deep iterative vessel segmentation in OCT angiography," *Biomedical Optics Express*, vol. 11, no. 5, pp. 2490–2510, 2020.
- [9] J. Zhang, Y. Qiao, M. S. Sarabi, M. M. Khansari, J. K. Gahm, A. H. Kashani, et al., "3D shape modeling and analysis of retinal microvasculature in OCT-Angiography images," *IEEE Trans. Med. Imaging*, vol. 39, no. 5, pp. 1335–1346, 2020.
- [10] M. Li, Y. Wang, Z. Ji, W. Fan, S. Yuan, and Q. Chen, "Fast and robust fovea detection framework for OCT images based on foveal avascular zone segmentation," *OSA Continuum*, vol. 3, no. 3, pp. 528–541, 2020.
- [11] Y. Lu, J. M. Simonett, J. Wang, M. Zhang, T. Hwang, M. Ahmed, et al., "Evaluation of automatically quantified foveal avascular zone metrics for diagnosis of diabetic retinopathy using optical coherence tomography angiography," *Investig. Ophthalmology Vis. Sci.*, vol. 59, no. 6, pp. 2212–2221, 2018.
- [12] M. Díaz, J. Novo, P. Cutrín, F. G. Ulla, M. G. Penedo, M. Ortega, "Automatic segmentation of the foveal avascular zone in ophthalmological OCT-A images," *Plos One*, vol. 14, no. 2, pp. 1–22, 2019.
- [13] M. Guo, M. Zhao, A. M. Y. Cheong, H. Dai, A. K. C. Lam, and Y. Zhou, "Automatic quantification of superficial foveal avascular zone in optical coherence tomography angiography implemented with deep learning," *Vis. Comput. Ind. Biomed., and Art*, pp. 2–21, 2019.
- [14] Y. Guo, A. Camino, J. Wang, D. Huang, T. S. Hwang, and Y. Jia, "MEDnet, a neural network for automated detection of avascular area in OCT angiography," *Biomedical Optics Express*, vol. 9, no. 11, pp. 5147–5158, 2018.
- [15] Y. Guo, T. T. Hormel, H. Xiong, B. Wang, A. Camino, J. Wang, et al., "Development and validation of a deep learning algorithm for distinguishing the nonperfusion area from signal reduction artifacts on OCT angiography," *Biomed. Opt. Express*, vol. 10, no. 7, pp. 3257–3268, 2019.
- [16] Y. Jia, S. T. Bailey, D. J. Wilson, O. Tan, M. L. Klein, C. J. Flaxel, et al., "Quantitative optical coherence tomography angiography of choroidal neovascularization in age-related macular degeneration," *Ophthalmology*, vol. 121, no. 7, pp. 1435–1444, 2014.
- [17] L. Liu, S. S. Gao, S. T. Bailey, D. Huang, and D. Li, "Automated choroidal neovascularization detection algorithm for optical coherence tomography angiography," *Biomedical Optics Express*, vol. 6, no. 9, pp. 3564–3575, 2015.
- [18] Q. Zhang, C. Chen, Z. Chu, F. Zheng, A. Miller, L. Roisman, et al., "Automated quantitation of choroidal neovascularization: a comparison study between spectral-domain and swept-source OCT angiograms," *Investig. Ophthalmology Vis. Sci.*, vol. 58, no. 3, pp. 1506–1513, 2017.
- [19] J. Xue, S. Yan, Y. Wang, T. Liu, F. Qi, H. Zhang, et al., "Unsupervised segmentation of choroidal neovascularization for optical coherence tomography angiography by grid tissue-like membrane systems," *IEEE Access*, vol. 7, pp. 143058–143066, 2019.
- [20] N. Takase, M. Nozaki, A. K. Kato, H. Ozeki, and Y. Ogura, "Enlargement of foveal avascular zone in diabetic eyes evaluated by enface optical coherence tomography angiography," *Retina*, vol. 35, no. 11, pp. 2377–2383, 2015.
- [21] J. Kang, R. Yoo, Y. H. Jo, and H. C. Kim, "Correlation of microvascular structures on optical coherence tomography angiography with visual acuity in retinal vein occlusion," *Retina*, vol. 37, no. 9, 2017.
- [22] S. A. Agemy, N. K. Sripsema, C. M. Shah, R. C. Gentile, Y. Hsiao, and Q. Zhou, "Retinal vascular perfusion density mapping using optical coherence tomography angiography in normals and diabetic retinopathy patients," *Retina*, vol. 35, no. 11, pp. 2353–2363, 2015.
- [23] M. Li, Y. Chen, Z. Ji, K. Xie, S. Yuan, Q. Chen, et al., "Image projection network: 3D to 2D image segmentation in OCTA images," *IEEE Trans. Med. Imaging*, vol. 39, no. 11 pp. 3343–3354, 2020.
- [24] A. F. Frangi, W. J. Niessen, K. L. Vincken, and M. A. Viergever, "Multiscale Vessel Enhancement Filtering," in *MICCAI*, 1998.
- [25] G. Azzopardi, N. Strisciuglio, M. Vento, and N. Petkov, "Trainable COSFIRE filters for vessel delineation with application to retinal images," *Med. Image Anal.*, vol. 19, no. 1, pp. 46–57, 2015.
- [26] J. Zhang, B. Dashtbozorg, E. Bekkers, J. P. W. Pluim, R. Duits and B. M. H. Romeny, "Robust retinal vessel segmentation via locally adaptive derivative frames in orientation scores," *IEEE Trans. Med. Imaging*, vol. 35, no. 12, pp. 2631–2644, 2016.
- [27] Q. P. Lau, M. L. Lee, W. Hsu, and T. Y. Wong, "Simultaneously identifying all true vessels from segmented retinal images," *IEEE Trans. Biomed. Eng.*, vol. 60, no. 7, pp. 1851–1858, 2013.
- [28] B. Sheng, P. Li, S. Mo, H. Li, X. Hou, Q. Wu, et al., "Retinal vessel segmentation using minimum spanning superpixel tree detector," *IEEE Trans. Cybern.*, vol. 49, no. 7, pp. 2707–2719, 2019.
- [29] E. Ricci and R. Perfetti, "Retinal blood vessel segmentation using line operators and support vector classification," *IEEE Trans. Med. Imaging*, vol. 26, no. 10, pp. 1357–1365, 2007.
- [30] S. Wang, Y. Yin, G. Cao, B. Wei, Y. Zheng, and G. Yang, "Hierarchical retinal blood vessel segmentation based on feature and ensemble learning," *Neurocomputing*, vol. 149, pp. 708–717, 2015.
- [31] Z. Yan, X. Yang, and K. T. Cheng, "A three-stage deep learning model for accurate retinal vessel segmentation," *IEEE J. Biomed. Heal. Informatics*, vol. 23, no. 4, pp. 1427–1436, 2019.
- [32] Q. Jin, Z. Meng, T. D. Pham, Q. Chen, L. Wei, and R. Su, "DUNet: A deformable network for retinal vessel segmentation,"

- Knowledge-Based Syst., vol. 178, pp. 149–162, 2019.
- [33] Z. Gu, J. Cheng, H. Fu, K. Zhou, H. Hao, Y. Zhao, et al., “CE-Net: Context encoder network for 2D medical image segmentation,” *IEEE Trans. Med. Imaging*, vol. 38, no. 10, pp. 2281–2292, 2019.
- [34] S. S. Gao, Y. Jia, L. Liu, M. Zhang, H. L. Takusagawa, J. C. Morrison and D. Huang, “Compensation for reflectance variation in vessel density quantification by optical coherence tomography angiography,” *Invest. Ophthalmol. Vis. Sci.*, vol. 57, no. 10, pp. 4485–4492, 2016.
- [35] Y. Ma, H. Hao, J. Xie, H. Fu, J. Zhang, J. Yang, et al., “ROSE: A retinal OCT-Angiography vessel segmentation dataset and new model,” doi: 10.1109/TMI.2020.3042802, 2020.
- [36] O. Ronneberger, P. Fischer, and T. Brox, “U-Net: Convolutional networks for biomedical image segmentation,” in *MICCAI*, 2015.
- [37] K. Li, X. Wu, D. Z. Chen, and M. Sonka, “Optimal surface segmentation in volumetric images - a graph-theoretic approach,” *IEEE Trans. Pattern Anal. Mach. Intell.*, vol. 28, no. 1, pp. 119–134, 2006.
- [38] M. K. Garvin, M. D. Abramoff, X. Wu, S. R. Russell, T. L. Burns, and M. Sonka, “Automated 3-D intraretinal layer segmentation of macular spectral-domain optical coherence tomography images,” *IEEE Trans. Med. Imaging*, vol. 28, no. 9, pp. 1436–1447, 2009.
- [39] B. Antony, M. D. Abramoff, L. Tang, W. D. Ramdas, J. R. Vingerling, N. M. Jansonius, et al., “Automated 3-D method for the correction of axial artifacts in spectral-domain optical coherence tomography images,” *Biomedical Optics Express*, vol. 2, no. 8, pp. 1734–1746, 2011.
- [40] Y. Zhang, C. Huang, M. Li, S. Xie, Z. Ji, K. Xie, et al., “Robust layer segmentation against complex retinal abnormalities for enface OCTA generation,” in *MICCAI*, 2020.
- [41] Y. Jia, O. Tan, J. Tokayer, B. Potsaid, Y. Wang, J. Jonathan, et al., “Split-spectrum amplitude-decorrelation angiography with optical coherence tomography,” *Optics Express*, vol. 20, no. 4, p. 4710, 2012.
- [42] Q. Chen, S. Niu, S. Yuan, W. Fan, and Q. Liu, “High-low reflectivity enhancement based retinal vessel projection for SD-OCT images,” *Med. Phys.*, vol. 43, no. 10, pp. 5464–5474, 2016.
- [43] M. D. Abramoff, M. K. Garvin, and M. Sonka, “Retinal imaging and image analysis,” *IEEE Rev. Biomed. Eng.*, vol. 3, pp. 169–208, 2010.
- [44] H. Wu, J. Zhang, and K. Huang, “FastFCN: Rethinking dilated convolution in the backbone for semantic segmentation,” arXiv:1903.11816, 2019.
- [45] L. Chen, Y. Zhu, G. Papandreou, F. Schroff, and H. Adam, “Encoder-Decoder with atrous separable convolution for semantic image segmentation,” in *ECCV*, 2018.
- [46] O. Oktay, J. Schlemper, L. L. Folgoc, M. Lee, M. Heinrich, K. Misawa, et al., “Attention U-Net: Learning where to look for the pancreas,” in *MIDL*, 2018.
- [47] Z. Zhou and M. R. Siddiquee, “UNet++: A nested U-Net architecture for medical image segmentation,” in *DLMIA*, 2018.
- [48] H. Huang, L. Lin, R. Tong, H. Hu, Q. Zhang, and Y. Iwamoto, “UNet 3+: A full-scale connected UNet for medical image segmentation,” in *ICASSP*, 2020.
- [49] C. S. Lee, A. J. Tyring, Y. Wu, S. Xiao, A. S. Rokem, N. P. De Ruyter, et al., “Generating retinal flow maps from structural optical coherence tomography with artificial intelligence,” *Sci. Rep.*, vol. 9, no. 1, 2019.
- [50] D. S. Kermany, M. Goldbaum, W. Cai, and M. A. Lewis, “Identifying medical diagnoses and treatable diseases by image-based deep learning resource identifying medical diagnoses and treatable diseases by image-based deep learning,” *Cell*, vol. 172, no. 5, pp. 1122–1124, 2018.
- [51] M. Alam, Y. Zhang, J. I. Lim, R. V. P. Chan, M. Yang and X. Yao, “Quantitative optical coherence tomography angiography features for objective classification and staging of diabetic retinopathy,” *Retina*, 2018.
- [52] H. Lee, M. Lee, H. Chung, H. C. Kim, “Quantification of retinal vessel tortuosity in diabetic retinopathy using optical coherence tomography angiography,” *Retina*, vol. 28, no. 5, pp. 876–985, 2018.
- [53] J. S. A. Romo, R. E. Linderman, A. Pinhas, J. Carroll, R. B. Rosen, T. Y. P. Chui, “Novel development of parafoveal capillary density deviation mapping using an age-group and eccentricity matched normative OCT angiography database,” *Transl. Vis. Sci. Technol.*, vol. 8, no. 3, 2019.
- [54] M. Zhang, T. S. Hwang, J. P. Campbell, S. T. Bailey, D. J. Wilson, “Projection-resolved optical coherence tomographic angiography,” *Biomedical Optics Express*, vol. 7, no. 3, pp. 816–828, 2016.
- [55] J. Wang, M. Zhang, T.S. Hwang, S. T. Bailey, D. Huang, D. J. Wilson, et al., “Reflectance-based projection-resolved optical coherence tomography angiography [Invited],” *Biomedical Optics Express*, vol. 8, no. 3, pp. 1537–1548, 2017.
- [56] Y. Liu, A. Carass, A. Filippatou, Y. He, S. D. Solomon, S. Saidha, et al., “Projection artifact suppression for inner retina in OCT angiography,” in *ISBI*, 2019.
- [57] A. E. Fayed, A. A. Fawzi, “Projection resolved optical coherence tomography angiography to distinguish flow signal in retinal angiomatous proliferation from flow artifact,” *Plos One*, vol. 14, no. 5, pp. 1–12, 2019.